



Article

Characterization of a Zn-Ca₅(PO₄)₃(OH) Composite with a High Content of the Hydroxyapatite Particles Prepared by the Spark Plasma Sintering Process

Jan Pinc^{1,2,*}, Jaroslav Čapek², Jiří Kubásek¹, Filip Průša¹ , Vojtěch Hybášek¹, Petr Veřtát², Ivona Sedlářová³  and Dalibor Vojtěch¹

¹ Department of Metals and Corrosion Engineering, University of Chemistry and Technology, Prague, Technická 5, 166 28 Prague, Czech Republic; kubasekj@vscht.cz (J.K.); Prusaf@vscht.cz (F.P.); hybasekv@vscht.cz (V.H.); Dalibor.Vojtech@vscht.cz (D.V.)

² FZU—Institute of Physics of Czech Academy of Sciences (CAS), Na Slovance 1999/2, 182 21 Prague, Czech Republic; capekj@fzu.cz (J.Č.); vertat@fzu.cz (P.V.)

³ Department of Inorganic Technology, University of Chemistry and Technology, Prague, Technická 5, 166 28 Prague, Czech Republic; Ivona.Sedlarova@vscht.cz

* Correspondence: pincj@vscht.cz; Tel.: +420-220-444-111

Received: 18 February 2020; Accepted: 11 March 2020; Published: 13 March 2020



Abstract: Zinc and zinc alloys have been studied due to their corrosion properties as potentially biodegradable materials. In this study, a zinc/hydroxyapatite composite (Zn/HA) containing 16 wt % HA was prepared by spark plasma sintering and characterized in detail. The microstructure, mechanical and corrosion properties were studied and the mutual relations between properties and microstructure were found. The porosity was evaluated to be approximately 18%. The mechanical properties (ultimate compression strength = 65 MPa and ultimate flexural strength = 120 MPa) are sufficient for the potential scaffolding and augmentation of cancellous bone. The flexural properties of these materials were measured for the first time. Immersion tests and subsequent analyses confirmed no direct participation of hydroxyapatite in the corrosion process and an ideal corrosion rate of approximately 0.4 mm/year. The amount of released zinc was between 4–6 mg/day corresponding with the maximal usable surface area of 25 cm². All the results suggest that the Zn/HA composite is suitable as a potential biodegradable material (from the point of view of mechanical and corrosion properties) for the replacement of cancellous bones.

Keywords: metal-matrix composites; biodegradable materials; sintering

1. Introduction

In recent years, zinc and zinc alloys have been intensively studied as potential biodegradable materials. Advantages of those materials are mainly connected to the corrosion process in comparison with metals like magnesium or iron [1]. Biodegradable metals/alloys must fulfill basic requirements for the use as an implant in the human organism. Suitable mechanical and corrosion properties, biocompatibility and non-toxicity of the elements present are the main ones. Therefore, essential elements naturally occurring in the human body, such as magnesium, iron or zinc, are studied as potential candidates for the fabrication of biodegradable metallic implants. Those metals are usually alloyed with other elements in order to adjust the properties of the material to the requirements of particular applications [2]. Fabrication of composites is another approach allowing enhancing of the mechanical properties of metallic materials [3,4]. In the case of biomaterials, hydroxyapatite (HA) is often used as a material matrix or reinforcement in composites, because it improves the biological interactions of the implant with the bone tissue [5].

Achieving similar or even the same structure and properties like the bone is quite difficult due to the many parameters participating in the preparation process of the materials and due to the complexity of the bone structure. One of the structural key factors of the biomaterials is porosity. Porosity inhibits the stress shield effect due to the decrease in the Young modulus compared to bulk materials, which have a higher Young modulus than human bones [6,7]. Porosity also affects the corrosion process through surface area changes [8]. Powder metallurgy processes, for example spark plasma sintering, allow the preparation of various materials with the desired structures. The final porosity can be adjusted by changing the characteristics (size, shape, etc.) of the initial powders and the sintering parameters (temperature, time and pressure) [9–12].

It is well known that the derivatives of hydroxyapatite form the inorganic part of the human bone tissue. The bone hydroxyapatite mostly contains other essential metallic elements, such as magnesium, sodium and minor amounts of other elements, for example potassium or zinc [13]. Those elements are incorporated in the HA structure instead of the calcium ions. The exact composition affects the solubility of hydroxyapatite, which is important for the usage of this material as a part of biodegradable metal based composites [14]. The presence of hydroxyapatite in implants enhances the proliferation of bone cells and the formation of new bone tissue as the consequence [15]. Due to those advantages, hydroxyapatite is used as a reinforcing filler of biocompatible composite materials [16,17] or coatings [18].

Biodegradable metallic composites based on an Mg or Fe matrix and HA reinforcement have been studied by several scientific teams and many studies focused on this topic have been published [19–22]. In contrast, according to our best knowledge, only one study concerning the Zn/HA composites was published [23]; even though Zn based alloys have been extensively studied as a potential biodegradable material [24–27]. Zinc is an essential element included in hundreds of proteins and enzymes, participating in many biological processes, such as bone mineralization or brain activity [28–30]. Compared with potential biodegradable metals like magnesium or iron, zinc has optimal corrosion properties [31,32]. The corrosion rate of metallic zinc lies between that of these metals and the corrosion process is not primarily connected with hydrogen evolution [33]. Another advantage of Zn based materials is, that antibacterial zinc oxide can theoretically be created in the structure [34,35] during their preparation. According to our knowledge, only one study concerning Zn/HA composites has been published [23]. Until now, zinc was predominantly used as a part of Mg/HA composites [36,37], of HA/Zn coatings [38,39] or of composites with a hydroxyapatite matrix [40,41].

This paper is focused on the preparation and characterization of Zn/HA16 wt % metallic matrix composites by spark plasma sintering. The high amount of HA was chosen to enhance the biocompatibility of prepared materials. Additionally, the corrosion properties were measured using immersion and electrochemical measurements in simulated body fluid (SBF). The obtained data was compared with that of similar materials (magnesium, magnesium and zinc composites) described in the available literature. Further on, it was compared with pure zinc, compacted under similar conditions as the composite, used as the reference material in this study. The obtained data provides a basic overview of the usability of Zn/HA composites in the field of biodegradable materials.

2. Materials and Methods

Powders of pure zinc (AlfaAesar, purity 99.9%, 44–105 μm) and of hydroxyapatite (HA) (Medicoat, 45–125 μm) were used as the initial materials. Both pure zinc and a mixture containing zinc and 16 wt % of HA were mixed and homogenized by a Turbula T2C mixer (WAB-GROUP, Muttens, Switzerland). The mixing of powders was performed in an air atmosphere, 30 min with 50 rotations per min. The conditions were used especially due to different densities of initial powders. Subsequently, the powders (pure zinc and the Zn/HA16 mixture) were compacted by spark plasma sintering (SPS) at 300 °C/10 min/10 kN using a HP D 10 furnace type. The compacts were of a cylindrical shape with a diameter of 20 mm and length of 5 mm. The cylinders were cut into two halves parallel to the compacting direction using a metallographic diamond blade and ground using P400–P4000 SiC

sandpapers. Polishing was carried out using a diamond paste (2 µm) and TOPOL 2 (Al₂O₃, 0.7 µm). Both the Zn and the Zn/HA composite were etched in a chromium solution (20 g CrO₃, 1.5 g Na₂SO₄ and 100 mL H₂O) in order to reveal the microstructure. Their microstructure was documented by an Olympus PME3 light metallographic microscope (LM; Olympus; Tokyo, Japan) and a TESCAN VEGA 3 LMU (SEM; TESCAN, Brno, Czech Republic) scanning electron microscope (SEM) equipped with an energy dispersive spectrometer OXFORD Instruments INCA 350 (EDX- Energy dispersive X-ray spectroscopy; AZtec, Oxford Instruments, Abingdon, United Kingdom).

The porosity of the prepared specimens was evaluated by three methods. The first method was a theoretical calculation based on the mass and dimensions of the prepared samples according to Equations (1) and (2).

$$\rho_{theor.} = \rho_{Zn} \cdot w_{Zn} + \rho_{HA} \cdot w_{HA} \quad (1)$$

$$\varepsilon = \left(1 - \frac{\rho_{real}}{\rho_{theor.}}\right) \cdot 100 \quad (2)$$

where ρ_{real} (real density) was calculated from the mass and volume obtained from external dimensions of the prepared samples and $\rho_{theor.}$ (theoretical density) was calculated by the sum of densities (ρ_{Zn} and ρ_{HA}) multiplied by weight fractions (w_{Zn} and w_{HA}) of the components. ε characterizes the theoretical porosity in percentage. The second method was the image analysis of LM and SEM micrographs, which was performed using ImageJ software. The third method was mercury porosimetry, which was performed using the Autopore IV 9500 V1.06 (Micromeritics, Unterschleissheim, Germany) equipment. This method was used for the direct measurement of the porosities and pore size distributions of both sintered samples and HA particles.

Compressive and flexural properties were measured using a universal testing machine LabTest 5.250SP1-VM (LABORTECH s.r.o., Opava, Czech Republic) at room temperature according to ASTM E9–19 Standard. Compressive tests were performed on three cuboid specimens with a side length of 5 mm and with a height of 7.5 mm. A loading rate of 0.3 mm/min was used (see Figure 1). In the case of the three-point bending test (ASTM E290–14), the dimensions of the three block samples were 18 mm × 4 mm × 4 mm and the loading rate of 1 mm/min was used (Figure 1). Hardness of the studied materials was measured by the Vickers method using a load of 5 kg (HV5).

For the corrosion tests, the samples were prepared in the same way as mentioned above. Subsequently, the cylinders were cut into two halves perpendicularly to the compacting direction (Figure 1) and ground with up to P2500 SiC papers. The tests were performed at 37 °C in simulated body fluid (SBF27) prepared according to Müller [42] (Table 1). The fluid contained NaN₃ (disinfection) and TRIS (buffer) too.

Table 1. Ion composition of simulated body fluid (SBF27; data from [42]).

Ions	Na ⁺	K ⁺	Ca ²⁺	Mg ²⁺	Cl [−]	HCO ₃ [−]	SO ₄ ^{2−}	HPO ₄ ^{2−}
(mmol/L)	142	5	2.5	1	109	27	1	1

The used volume ratio of the SBF solution to the surface area of the samples was 80 mL/cm². After the exposition, corrosion products were analyzed by a PANalytical X'Pert PRO powder diffractometer with a Co anode ($\lambda = 0.1789$ nm) in a Bragg–Brentano geometry (XRD; PANalytical, Holland) and documented by scanning electron microscope (SEM–EDX). After that, the corrosion products, formed on the material surface, were chemically removed by a chromium oxide solution (200 g/L CrO₃, 10 g/L AgNO₃, and 20 g/L Ba(NO₃)₂, at 25 °C). The cross sections of corroded samples were examined by the SEM–EDX. The corrosion rate was calculated according to ASTM G31-72

(Equation (3)), where A is the area (cm^2), D is the density (g/cm^3) and t is the time (h). The values m_i and m_f are characterized as initial and final weights of the samples.

$$v_{\text{cor.}} = 87.4 \times \frac{(m_i - m_f)}{(ADt)} \quad (3)$$

The 2 mL of HNO_3 was added into the SBF solution after exposition, and the concentration of released ions were analyzed from the solution using an AGILENT 280 FS AA SPECTROMETER (AAS; Agilent Technologies, Australia). The obtained concentrations (mg/L) were recalculated to ($\text{mg}/\text{cm}^{-2}\cdot\text{day}$) using the volume, area and the number of days.

The corrosion behavior of the prepared samples was also measured by electrochemical methods (polarization resistance and potentiodynamic polarization) using a potentiostat Gamry Reference600 (Gamry, Warminster, Pennsylvania). The scanned potential interval was -0.02 to $+0.02$ V and the scanning rate was 0.125 mV/s for the measurements of polarization resistance and -0.05 to $+1.00$ V and 1 mV/s for the potentiodynamic polarization measurements. The measurements were performed using a standard three electrode setup—an Ag/AgCl (SSCE) and a graphite electrode, which were used as the reference and the counter electrode respectively. The electrochemical measurements were performed in simulated body fluid (Table 1) at a temperature of 37°C . The corrosion rates were evaluated from the polarization resistance.

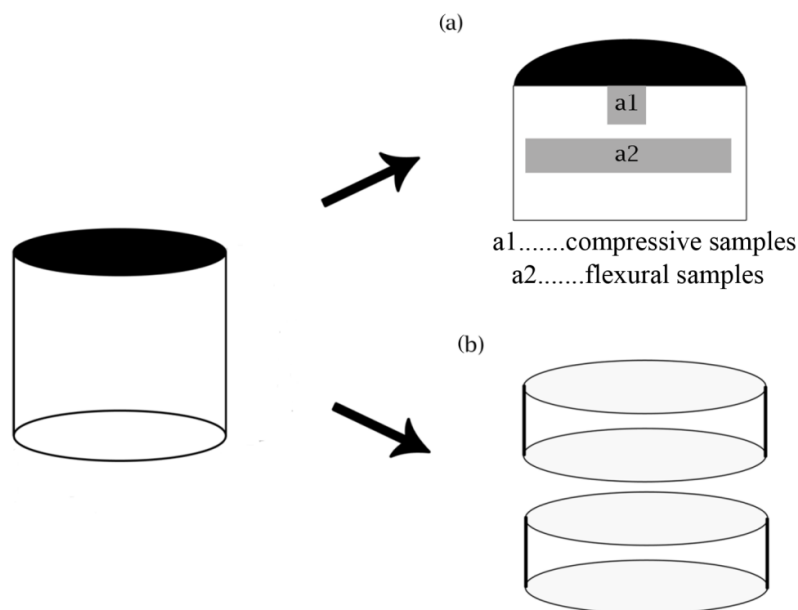


Figure 1. Shape and locations of the samples intended for the characterization of (a) the microstructure, (a1) compressive, (a2) flexural and (b) corrosion properties.

3. Results and Discussion

3.1. Microstructure

Morphologies of the starting powders, i.e., zinc and hydroxyapatite (HA), are shown in Figure 2. The zinc powder consisted of elongated particles with a diameter of $50\text{--}150\text{ }\mu\text{m}$ and a length of $100\text{--}500\text{ }\mu\text{m}$. Besides those elongated particles, a minor amount of the Zn spherical particles with a diameter ranging between 40 and $105\text{ }\mu\text{m}$ was observed as well (Figure 2a). The hydroxyapatite powder particles were characterized by an irregular, sharp-edged shape and significant porosity with the average pore size $1\text{ }\mu\text{m}$ (see the detail in Figure 2b). The size of the HA particles ranged from 20 to $200\text{ }\mu\text{m}$ (Figure 2b). The morphology and grain size of particles were not changed after the mixing due to the conditions of mixing and character of the materials.

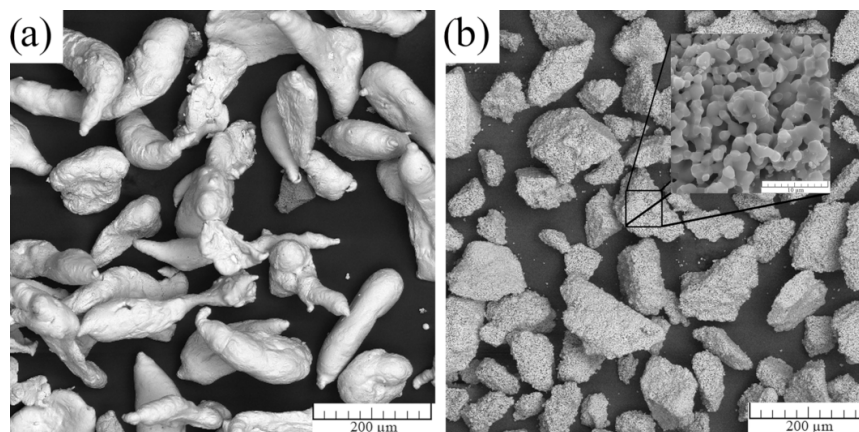


Figure 2. Morphology of the initial powders: (a) zinc and (b) hydroxyapatite.

One of the crucial properties of the biodegradable materials is the porosity of the prepared material. The porosity significantly affects the overall performance of the material, and it is critical to define the exact influence on individual biodegradable material. The porosity of the used HA particles was estimated by the mercury porosimetry (Figure 3) was 15 vol.%. In Figure 3, the green curve represents the cumulative intrusion, which is defined as the volume of intruded mercury at each measured pressure. The red curve is defined as the $dV/d\log R$ pore volume. It is obvious that the determination of the porosity by mercury porosimetry is difficult in the case of powders because the peaks belonging to the interparticle space can overlap with those belonging to the pores of the particles. Fortunately, in this measurement, the peaks were clearly distinguishable (see Figure 3). Namely, the first peak was connected with the interparticle space and the second with the porosity of the HA particles. It means that the pore size radius ranged approximately from 0.1 to 1 μm .

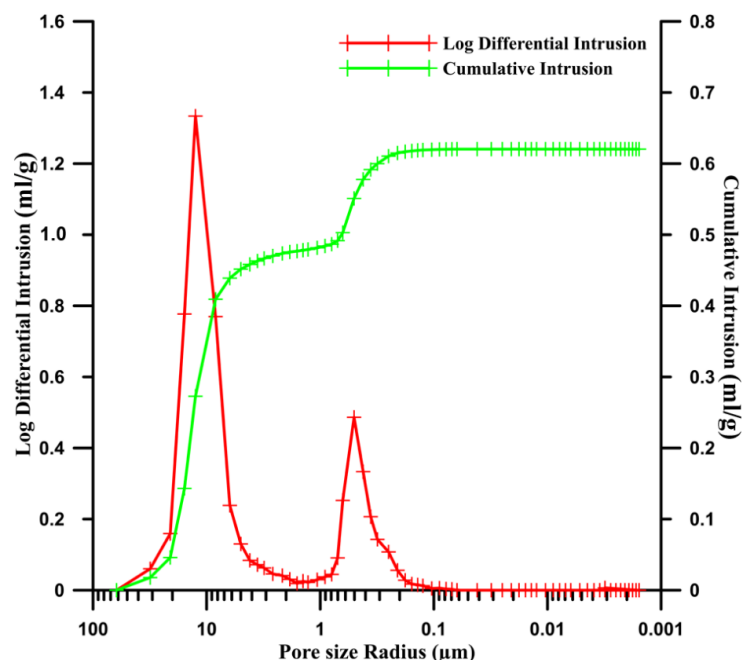


Figure 3. Measurement of the porosity of the hydroxyapatite particles with two distinguished peaks representing the interparticle space (first peak) and particle porosity (second peak).

Figure 4 shows the microstructures of the Zn/HA composite and sintered Zn. In the case of the Zn/HA composite, the HA particles were distributed quite homogeneously in the Zn matrix (Figure 4a) and the HA content was estimated to be of approximately 32 vol.% based on the measurement of the

area fraction by the image analysis. At higher magnification (Figure 4b), some pores were observed as well. Those pores occurred predominantly between neighboring HA particles and between HA particles and Zn matrix. Those pores were irregular in shape and possessed sharp edges and a size of approximately 20–50 μm . Their origin can be ascribed to the negligible diffusion between Zn–HA and HA–HA particles. A significant contribution to the formation of the Zn–HA pores can be also found in the annihilation of the Zn–Zn pores during the SPS process. The pore annihilation is connected with the contraction of the zinc matrix [43], which can lead to a breakage of the weak mechanical (diffusion less) bonds between the Zn and HA particles. The diffusion between the neighboring HA particles was very limited because of the low sintering temperature. In the case of the Zn matrix, only a negligible porosity consisting of very small pores (diameter of about 1 μm in average) was observed (Figure 4b). The microstructure of pure zinc consisted of a large number of small pores (up to 20 μm), which occurred predominantly on the triple junctions of the grains is shown in Figure 4c.

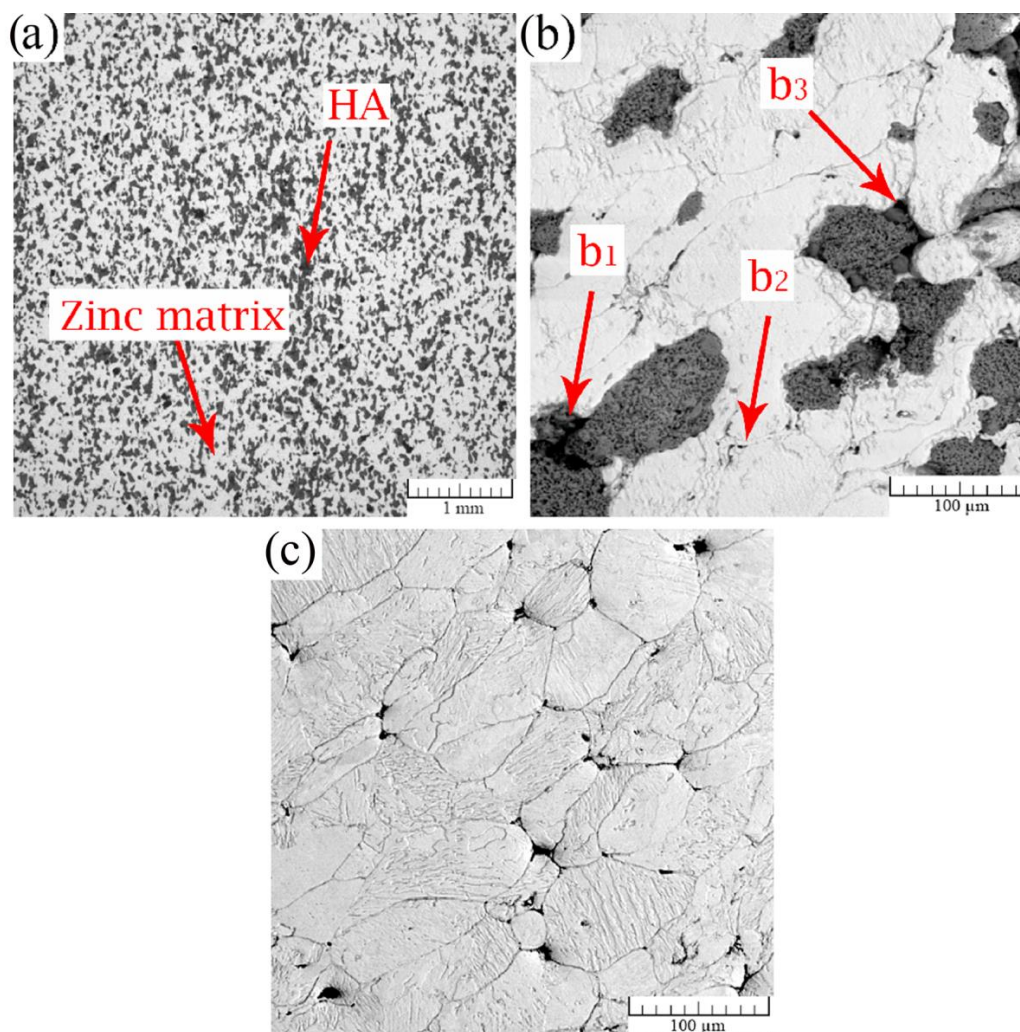


Figure 4. Light metallographic microscope (LM) micrographs of the cross-sections of (a,b) Zn/HA16 and (c) Zn samples. In the image (b), pores occurring between HA–HA (b1), Zn–Zn (b2) and Zn–HA (b3) particles are pointed out.

Table 2 summarizes porosities and average pore sizes obtained by various methods. In the case of the Zn/HA composite, the zinc matrix data includes the porosity, which occurred between Zn–Zn particles as well as between Zn–HA particles due to the indistinguishability of those pores by the image analysis. According to Equations (1) and (2) the porosity of the Zn/HA composite was 18 vol.% and that of Zn was 2.7 vol.%. The porosity of 18% was divided into the contributions of the individual

components based on their volume ratios (Table 2) according to Equation (4). Where ε_{HA} is a porosity, which is formed by the HA in the Zn/HA16 composite with the composition 30 vol.% HA ($= \varphi_{HA}$) and 70 vol.% Zn. The value $\varepsilon_{Zn/HA16}$ is the porosity of the whole composite (18 vol.%). The recalculation was also used for the mercury porosimetry measurement in order to compare the accuracies of the individual methods. It is obvious that the porosity between Zn and HA particles formed the majority of the material porosity and the values obtained by those two methods were similar.

$$\varepsilon_{HA} = \varphi_{HA} \cdot \varepsilon_{\frac{Zn}{HA16}} \quad (4)$$

Table 2. Average pore size and porosity of pure zinc and zinc composite evaluated by different methods.

Sample	Theoretical Porosity	Porosity Evaluated by Image Analysis	Porosity Evaluated by Mercury Porosimetry	Average Pore Size (μm)
Pure zinc	2.7%	1.7%	5%	21
Zinc matrix	12.6%	18%	10.2%	<1 (Zn–Zn) ~19 (Zn–HA)
HA	5.4%		4.6%	

It is clearly visible in Table 2 that the porosity of HA particles evaluated by the theoretical calculation was close to the value obtained by the mercury porosimetry measurement (Table 2). Together with a low sensitivity of the image analysis and its relatively high inaccuracy for the porosity determination (standard deviation 2.5 vol.%), the theoretical calculation and the mercury porosimetry seem to be more precise methods for the evaluation of Zn/HA16 porosity. Estimating the Zn/HA composite porosity by the image analysis from light micrographs was not possible, because both HA particles and pores appear dark in them and were not distinguishable as a consequence.

Therefore, we acquired EDX data and created X-ray elemental maps of Zn, Ca, P and O and overlapped them (Figure 5). Subsequently, black (pores) and white (Zn and HA) pictures were obtained in that way and were subjected to the image analysis. As the result, we obtained an average pore size of 19 μm and porosity of 10.2 vol.%. The difference between the porosities obtained according to the Equation (1) and image analysis was caused by the porosity of the HA particles (Figure 2b), which was not taken into account when the image analysis was performed. That was due to a small size of those pores, which was under the resolution of the EDX analysis.

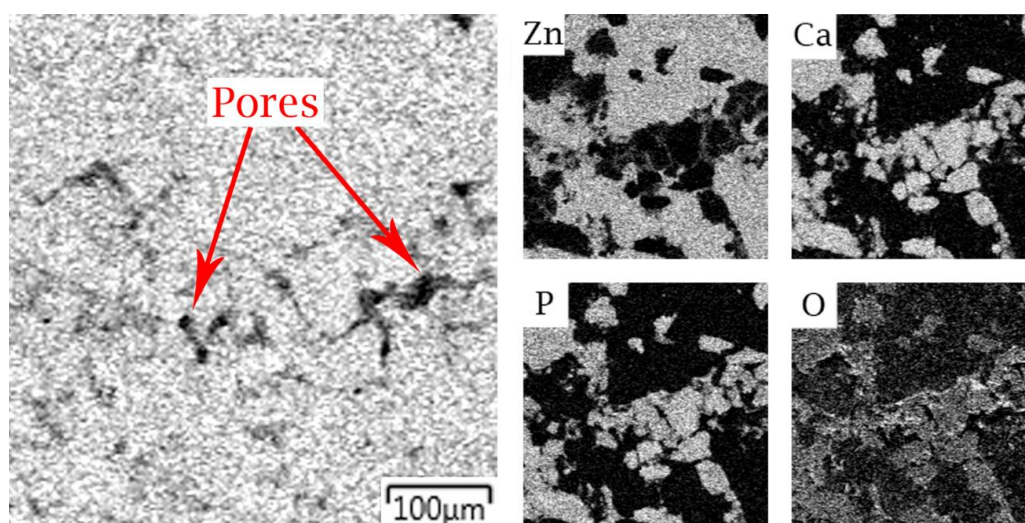


Figure 5. Overlapped EDX maps of the Zn/HA composite for the porosity analysis.

We also tried to use mercury porosimetry to estimate the porosity of the Zn/HA composite and the sintered zinc (Figure 6). Unfortunately, the results for the sintered specimens were affected by the volume changes of the samples, which were caused by the reaction of zinc with mercury and the formation of an amalgam. The volume changes were characterized by the fluctuation of the log differential intrusion curves and it was visible especially in the case of pure zinc (Figure 6). It can be also seen in Table 2 that the value of pure zinc porosity evaluated by mercury porosimetry was higher in comparison with the image analysis or theoretical calculations, while the value for the Zn/HA composite showed an opposite trend. These changes were caused by the different amount of exposed zinc and time of exposition. It means that we must reach a higher pressure in the case of the Zn/HA composite to ensure the contact with zinc inside the material. Due to the fact that the “contact” time was shorter, as well as the amount of exposed zinc and the volume changes were minimal in comparison with pure zinc.

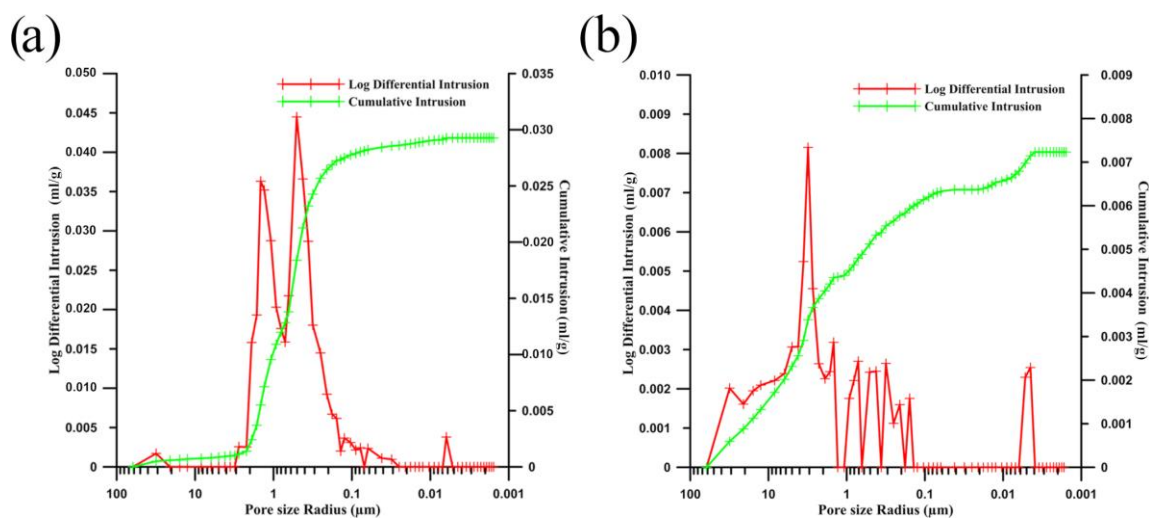


Figure 6. Porosity measurement of (a) the zinc composite with a characteristic second peak for HA particles porosity (0.1–1 μm) and (b) pure zinc with visible volume changes during the measurement.

Compared with the Zn matrix in the Zn/HA composite, the pure sintered zinc contained larger pores occurring predominantly on the contacts of the three particles (see Table 2 and Figure 4). However, the total porosity of the composite was higher due to the porosity of the HA particles. The average pore size of the pure zinc was 21 μm , the theoretical porosity calculated according to Equation (1) was 2.7 vol.% and the porosity obtained by the image analysis as a pore area fraction was 1.7 vol.%. Considering the inaccuracy of both methods, we could claim that those values were consistent. The higher porosity of the pure Zn compared to that of the Zn matrix in the Zn/HA composite could be explained by a different dissipation of the compaction energy in different powder mixtures. In the case of pure zinc, part of the compaction energy was consumed by the plastic deformation of ductile zinc particles during the pressing. On the other hand, in the case of the Zn–HA mixture, the HA particles were not plastically deformed, i.e., their deformation consumed only a small amount of the compaction energy and a larger amount of this energy was applied on the zinc particles as a consequence. Moreover, the mixture contained a lower amount of the highly deformable zinc particles; therefore, they could be plastically deformed to a higher degree, which led to the formation of a lower number and smaller size of the pores. Moreover, the HA particles acted as stress concentrators and improved compacting in their vicinities as a consequence. A similar effect, the addition of hard particles into metallic mixtures, on the density of metallic matrix was observed in [44].

Figure 7 shows the etched microstructure of pure zinc observed in a polarized light. It is clearly visible in Figure 7 that the surfaces of the initial powder particles were etched preferentially. It is a commonly observed phenomenon occurring if powder metallurgical samples are chemically etched

and is usually ascribed to the preferential etching of the oxides surrounding the particles. However, we did not observe any oxidic envelopes, neither by XRD nor by EDX, most likely because of their low thickness. Despite that, their presence can be assumed because zinc is not a noble metal and an oxidic layer is formed on its surface when it is in contact with the atmosphere. Despite this issue, the microstructure of the individual particles was successfully etched and the grain size ranged from several units to several tens of micrometers. In Figure 7, the pores are colored in green. The grain size of the individual zinc particles in the Zn/HA composite was comparable with that of pure zinc.

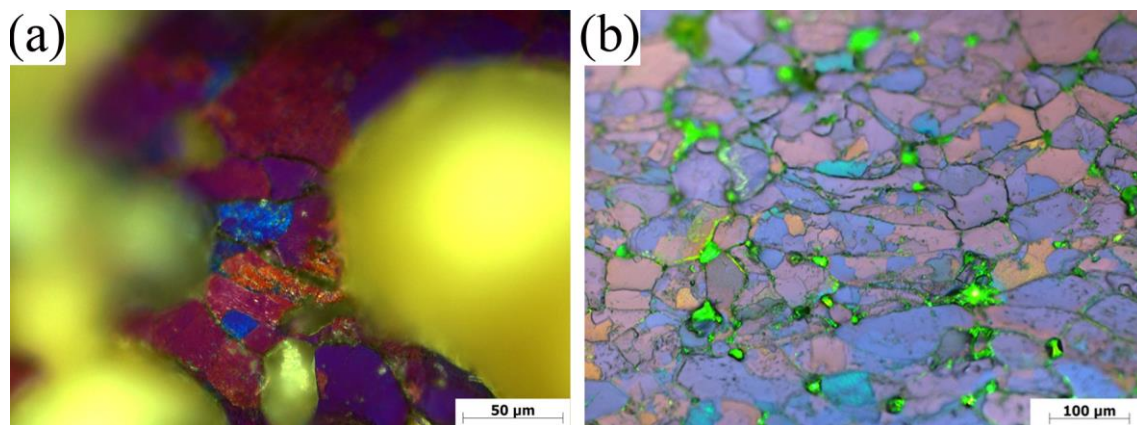


Figure 7. The microstructure of Zn/HA (a) pure zinc (b) in polarized light. Pores are colored in yellow and green. Individual grains are visible inside individual zinc particles.

3.2. Mechanical Properties

In this study, compressive and flexural properties were measured. The flexural properties were measured for the first time for the Zn/HA composite to the best of our knowledge. Engineering stress–strain curves obtained by the compression and flexural tests of the pure zinc and Zn/HA composite are shown in Figure 8 and the important values obtained from these curves, as well as hardness HV 5, are listed in Table 3. Generally, it is clearly visible in Figure 8 that the deformation of the Zn/HA composite was accompanied by only a negligible plastic deformation, while pure zinc deformed plastically during the flexural test. However, some plastic deformation of the Zn/HA composite was observed in compression, which is an important property for the compressive loaded materials. From Table 3, it is obvious that the addition of the HA particles strongly deteriorated mechanical properties of the material. That can be explained by the presence of the HA particles, which acted rather as defects than reinforcements because of a weak or no bonding of the HA particles with the Zn matrix (see Figure 4). As the result, the fracture spread through the HA–HA and HA–Zn interfaces, which is clearly visible in SEM micrographs of the fracture surfaces obtained by the flexural test (Figure 9). The HA fraction obtained by the image analysis of the BSE–SEM micrographs of the fracture surface (Figure 9a) was approximately 64%, which is two times higher than that observed on metallographic cross-sections (Figure 4a). It proves that the fracture spread through the HA–HA and HA–Zn interfaces preferentially. Due to that, it could be assumed that with an increasing content of HA, the ultimate flexural strength would decrease. At a higher magnification (Figure 9b), only a low number of plastically deformed regions were found. This resulted in the fragile behavior of the Zn/HA composite (see Figure 8). In both cases (pure zinc and Zn/HA composite), the signs of plastic deformation were connected with a trans-granular fracture. The deteriorated particle cohesiveness of the Zn/HA composite influenced the hardness negatively too (see Table 3).

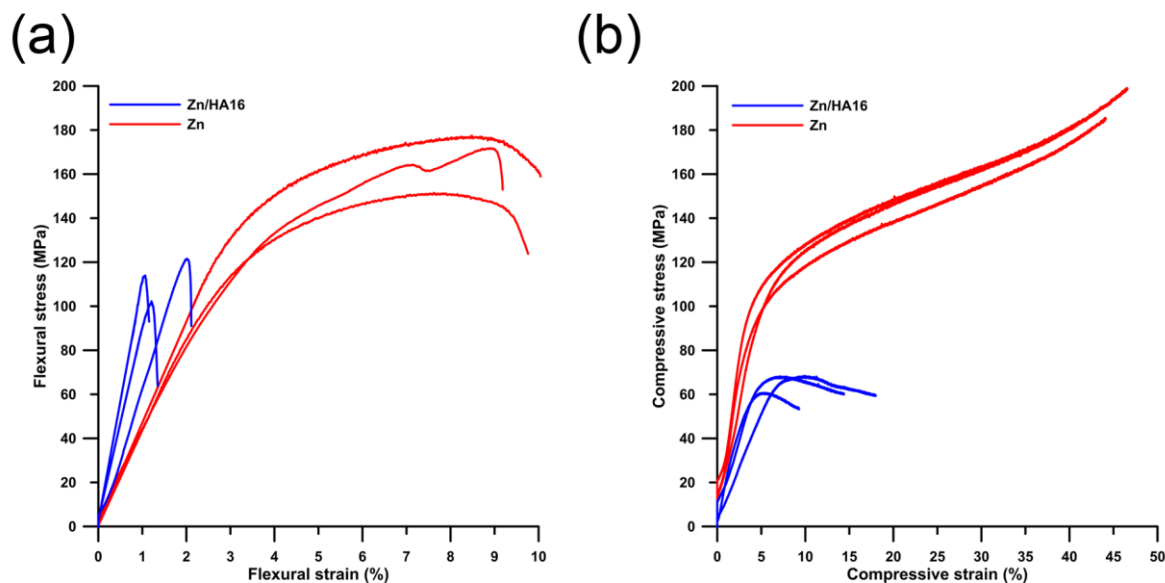


Figure 8. Engineering stress–strain (a) flexural and (b) compressive curves.

Table 3. The overview of mechanical properties (average values) of selected biodegradable materials and the human bone.

Materials	UFS (MPa)	Hardness (HV)	CYS (MPa)	UCS (MPa)	Reference
Cortical bone	160	-	-	88–230	[45,46]
Cancellous bone	-	-	2–12	0.2–80	[47,48]
PM Zinc	167 ± 11	33 ± 2 (HV5)	81 ± 5	-	This study
PM Magnesium	9	27 (HV 3)	33	45	[48]
Zn/1HA *	-	46 (HV0.1)	70	157	[23]
Zn/5HA *	-	45 (HV0.1)	42	109	[23]
Zn/10HA *	-	45 (HV0.1)	47	72	[23]
Zn/16HA	113 ± 8	24 ± 5 (HV5)	46 ± 3	65 ± 4	This study
Mg/5HA	-	64 (HV1)	205	330	[49]

*—Vickers hardness measured just for the zinc matrix, PM—powder metallurgy, UFS—ultimate flexural strength, CYS—compressive yield strength, UCS—ultimate compression strength.

Although we found that the addition of HA led to a decrease in the mechanical properties of zinc, it did not necessarily have a negative impact on the potential usability of the Zn/HA composite. From Table 3, where the mechanical properties of the human bone and various biomaterials are listed, it is obvious that the mechanical properties of the prepared composite were generally higher than these of the cancellous bone. In [23], and in [45] it was observed too, that the HA in various types of composites can also deteriorate their mechanical properties without any negative impact on the usability. If we compared the properties of the Zn/HA composite prepared in this study with those prepared by Yang et al. in [23], we did obtain comparable values of mechanical properties at a larger amount of added HA, which should be beneficial from the biological point of view.

Mechanical properties of the Zn/HA composite and pure zinc prepared by SPS were compared with those of the Zn/HA composites (1 wt %, 5 wt % and 10 wt %) and magnesium-based materials obtained from the literature (Table 3). All compared materials were prepared by the spark plasma sintering process. However, initial particle sizes of used powders were different, as well as the sintering conditions. In the case of the Zn composites (1 wt %, 5 wt % and 10 wt %), nano-sized hydroxyapatite powders were used. Those particles formed agglomerates, which means that the microstructure was similar to that of the composite prepared in this study (using HA particles with the size of several tens of micrometers). Compression yield strength (CYS) of Zn/HA with 16 wt % of hydroxyapatite is comparable with that of the zinc composites with a lower content of HA prepared in [23] and with pure

PM magnesium. It can be seen in Table 3 that the value of the ultimate compression strength decreases with the rise of the HA content. The UCS decrease is connected mainly with the lower amount of diffusion connections between zinc particles due to the HA presence, which was mentioned above. Lower values of the Vickers hardness were caused by the fact that we measured the hardness of both components (Zn matrix + HA) instead of the zinc matrix as was measured in [23].

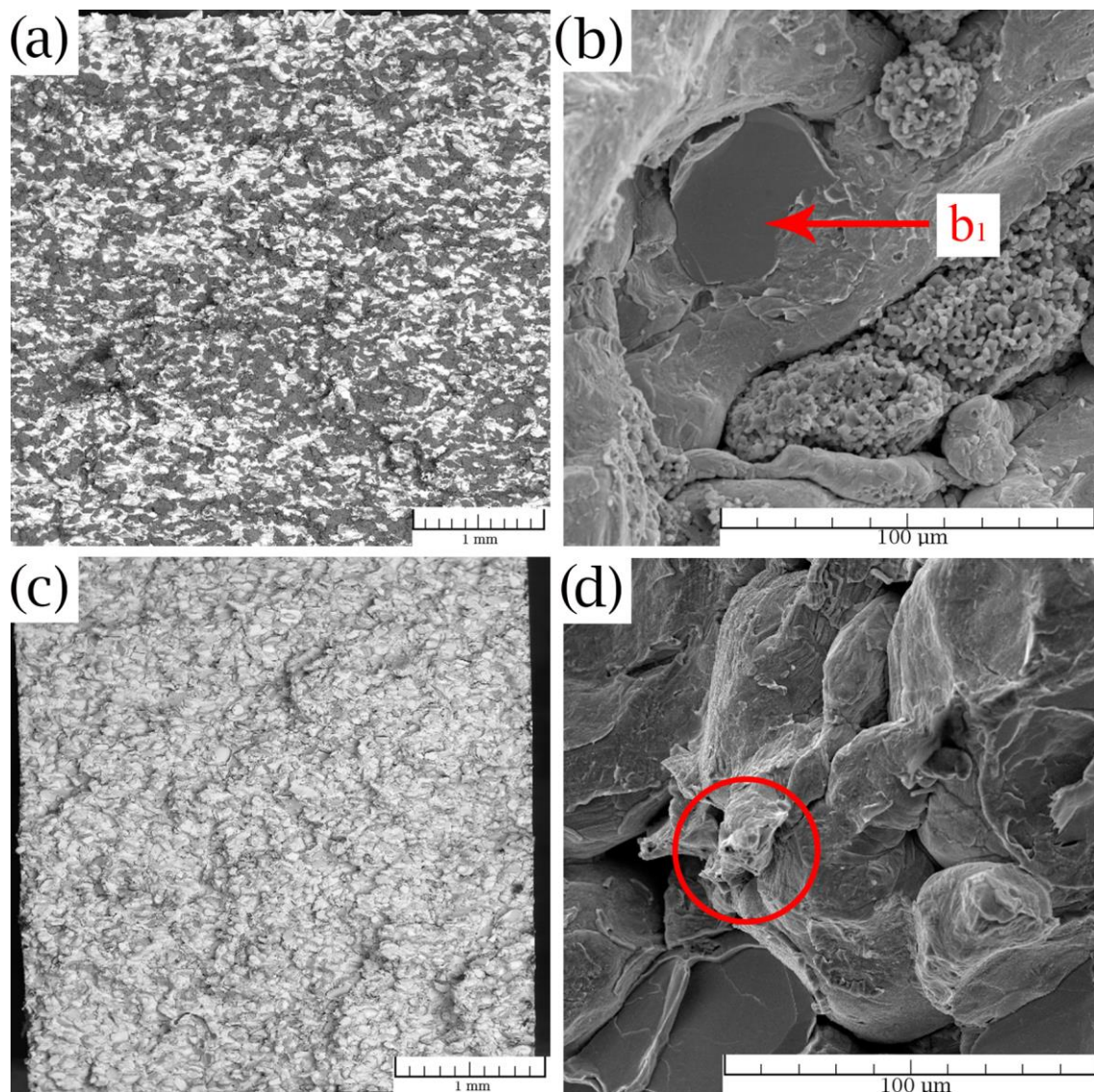


Figure 9. Fracture surfaces of (a,b) the sintered composite Zn/HA16 with a pointed trans-granular fracture (b1) and (c,d) pure zinc with the highlighted sign of plastic deformation.

3.3. Corrosion Properties

The immersion tests were performed in the simulated body fluid (SBF) for a period of 14 days. The corrosion rates were evaluated by weight loss and ion release and are summarized in Table 4. It can be seen in Table 4 that the corrosion rate of the Zn/HA composite was higher than that of zinc. The higher value of the corrosion rate can be explained by the acceleration of the corrosion process by the increase of the exposed area due to higher surface porosity (Figures 2 and 3). The corrosion process, with high probability, can also be affected by the sorption of Zn^{2+} ions by HA [50]. As a consequence of the sorption process, the electric properties (proton conductivity) of HA and the amount of Zn ions in the solution can be changed [51]. Due to that, the corrosion rate of the Zn/HA composite can be

accelerated compared with pure zinc. It is important to mention that the mechanism of this process is quite difficult and still not fully understood. In order to explain the corrosion process, we observed and documented the sample surface after chemically removing the corrosion products (see Figure 10a) and we found that a lot of HA particles were released from the sample surface after etching the corrosion products. It means that the weight losses listed in Table 4 did not include only the weight changes caused by the corrosion of the zinc matrix but also the weight losses caused by the HA release after the etching. Due to that the weight gains were also calculated and it was found that the gains were in the case of the Zn/HA composite significantly higher (2.5% for Zn/HA and 0.5% for the zinc). It confirmed the higher corrosion rate of the Zn/HA composite.

Table 4. Corrosion rates evaluated from the weight loss, ion release and polarization resistance measurement.

Methods	Weight Loss		AAS	Polarization Resistance	
	mm/year	mg/(cm ² ·day)		mm/year	mg/(cm ² ·day)
Samples					
SPS Zinc	0.26	0.45 ± 0.05	0.40 ± 0.03	0.85	1.72 ± 0.18
SPS Zn/HA16 composite	0.41	0.54 ± 0.04	0.45 ± 0.07	1.52	2.81 ± 0.35

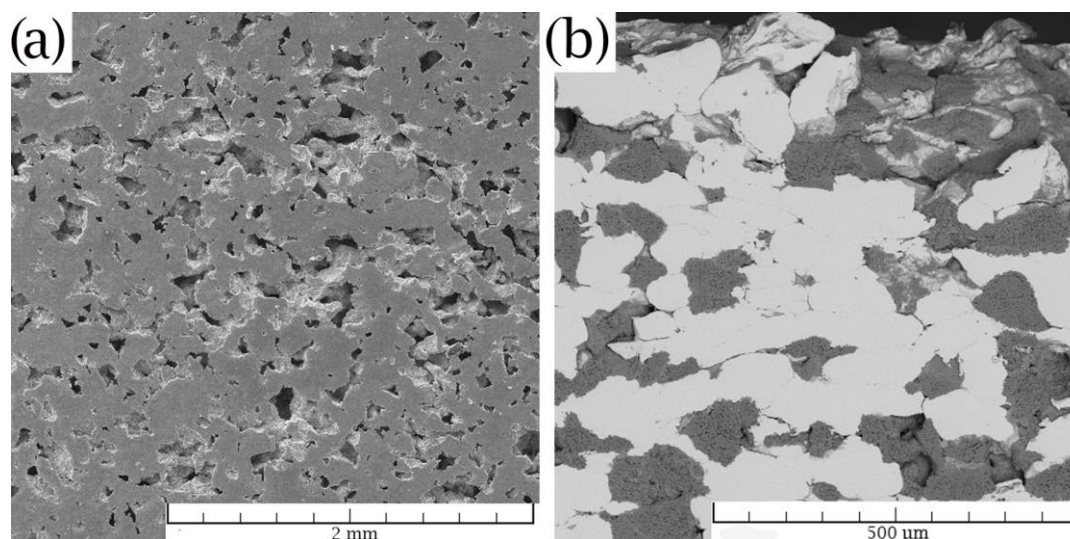


Figure 10. Surface of the Zn/HA composite after the pickling (a) of the corrosion products and (b) cross-section surface after the corrosion test.

Although the penetration of the corrosion medium through the Zn/HA composite can be expected and was even observed, because of the interconnected network of porous HA particles, no significant corrosion was observed inside the material (Figure 10b). This could be explained by the limited diffusion of oxygen through the pores with a very small pore size (0.1–1 μm). This caused an oxygen deficiency hindering the corrosion attack.

Atomic absorption spectroscopy showed relatively similar results of ion release per day for both materials. The value decrease can be caused, in the case of the Zn/HA composite, by the zinc ion sorption mentioned above. The amount of corroded zinc, determined from the weight loss was 4.9 mg/day for zinc and 5.5 mg/day for the Zn/HA composite. This is approximately one-third of the recommended dietary allowance for adults (15 mg/day) [52]. It means that the maximal usable surface areas were 29 cm² for zinc and 24 cm² for the Zn/HA composite. The surface areas of both samples were approximately 9 cm².

During the exposition, the pH value raised from 7.7 to 8.4. The pH stabilized on the pH value 8.4 for the last 3 days of the exposition, which is most likely connected with reaching an equilibrium state. No significant differences between the pH evolution of sintered zinc and zinc composite were observed.

In the case of the Zn/HA composite, the zinc particles corroded around the HA particles predominantly, which was confirmed by the release of HA particles during the etching (Figure 10a). The distribution and structure of corrosion products on the samples are shown in Figure 11. The distribution of corrosion products was quite inhomogeneous. In the case of the Zn/HA composite, the corrosion products were accumulated mainly between the HA particles and the zinc matrix. It means that those products fixed the HA particles in the structure of the composite. The structures of corrosion products were very similar for both samples.

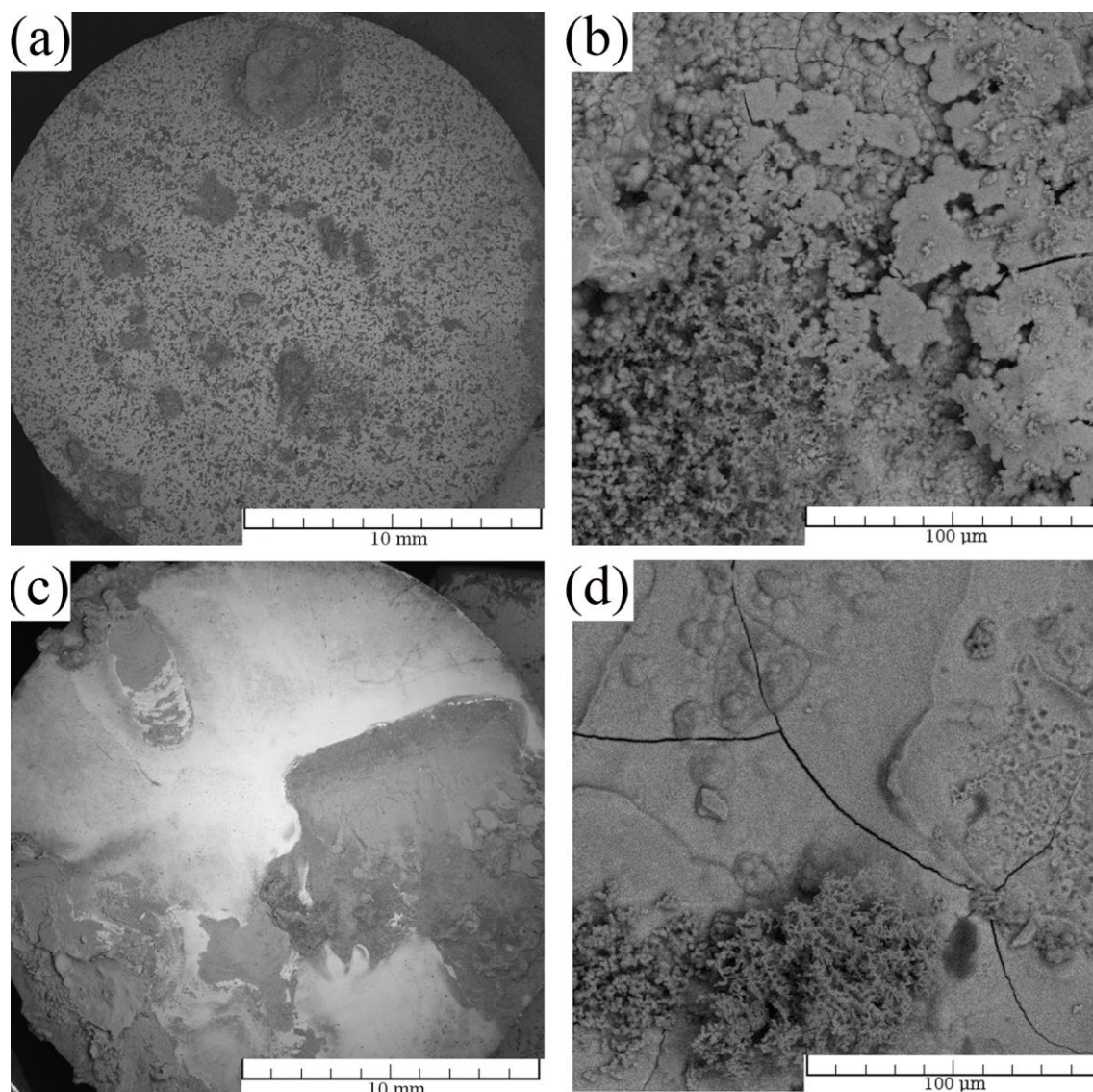


Figure 11. Corrosion products on the surface of corroded (a,b) Zn/HA and (c,d) Zn.

The composition of the corrosion products was analyzed by EDX and XRD. Elemental distribution of the corrosion products measured by EDX is shown in Figure 12. In addition to the original elements occurring in the Zn/HA composite (Zn, Ca, P and O), chlorine and carbon were also present in the corrosion products. The composition of the corrosion products of the Zn/HA was evaluated as simonkolleite ($\text{Zn}_5(\text{OH})_8\text{Cl}_2 \cdot \text{H}_2\text{O}$), hydrozincite ($\text{Zn}_5(\text{CO}_3)_2(\text{OH})_6$), hydroxyapatite ($\text{Ca}_5(\text{OH})(\text{PO}_4)_3$) and pure Zn by XRD. The presence of hydroxyapatite can be described in two different ways. The first, it was the HA from the sample (similarly as the pure zinc) and second, the HA precipitated from the solution. It is well known, that the hydroxyapatite in the structure of a material can have a significant effect on the precipitation of HA from the SBF [53]. The same phase composition, except for

hydroxyapatite, was found in the case of the corrosion products on the sintered zinc. Although no phosphates were found in the corrosion products by XRD, their presence in amounts under the detection limit cannot be excluded [54]. Together with the results obtained by EDX analysis (confirmation of ratio between individual elements) and the literature concerning biodegradable zinc [54] (confirmed the presence of only crystalline products during the degradation of zinc in SBF), the presence of the above-mentioned corrosion product can be expected.

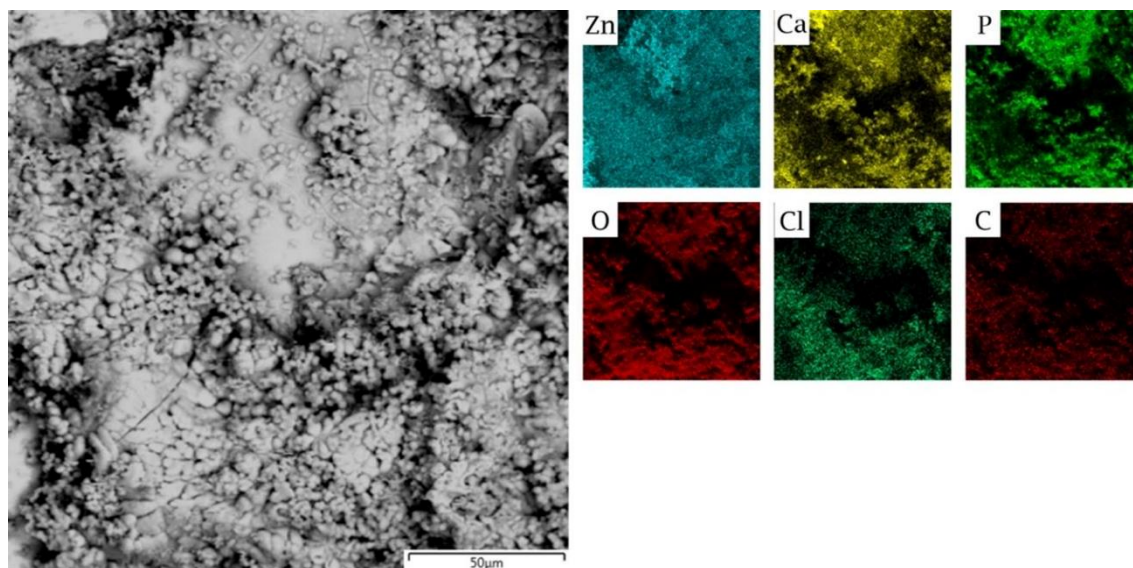
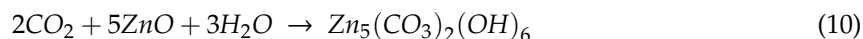
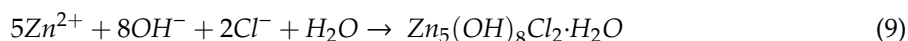


Figure 12. X-ray elemental distribution of the corrosion products on the Zn/HA composite (SEM–EDX).

The corrosion process of zinc in simulated body fluid was described by Liu et al. [53] in detail and their results connected to the corrosion rate and pH changes are in good agreement with our study. The change of pH was caused by the corrosion process, which is connected with the generation of OH^- ions by the depolarization (cathodic) reaction (Equation (6)). Based on the composition of corrosion products and pH increase, the electrochemical process can be described according to the equations (Equations (5)–(10)) [54–56]:



The electrochemical measurements in simulated body fluid confirmed a higher corrosion rate of the Zn/HA composite. The value of corrosion rates evaluated by the polarization resistance was 0.9 mm/year and 1.5 mm/year for zinc and the Zn/HA composite respectively. These corrosion rates are significantly higher than those obtained by the immersion tests because the polarization resistance characterizes the corrosion rate only in the initial stage of the corrosion process. In this stage, the corrosion rate is usually significantly higher than the average long-term corrosion rate. Potentiodynamic curves were also measured and are shown in Figure 13. In Figure 13 it is clearly visible that the mechanism of the corrosion process of both materials was the same and that HA played no or a negligible role on the corrosion process. The curves in Figure 13 did not show the fluctuations characteristic for the crevice corrosion [57]. Fluctuations on the anodic curves were rather connected

with the creation of an oxide layer. Since the contact areas between the metal and electrolyte differed and the exact exposed areas were unknown to us, we were not able to determine the exact corrosion rates from the potentiodynamic curves, however, they were very helpful to clarify the corrosion mechanism. Together with the information mentioned above, it can be assumed that the main reason of the higher corrosion rate of Zn/HA was caused by a higher exposed area of the Zn/HA samples.

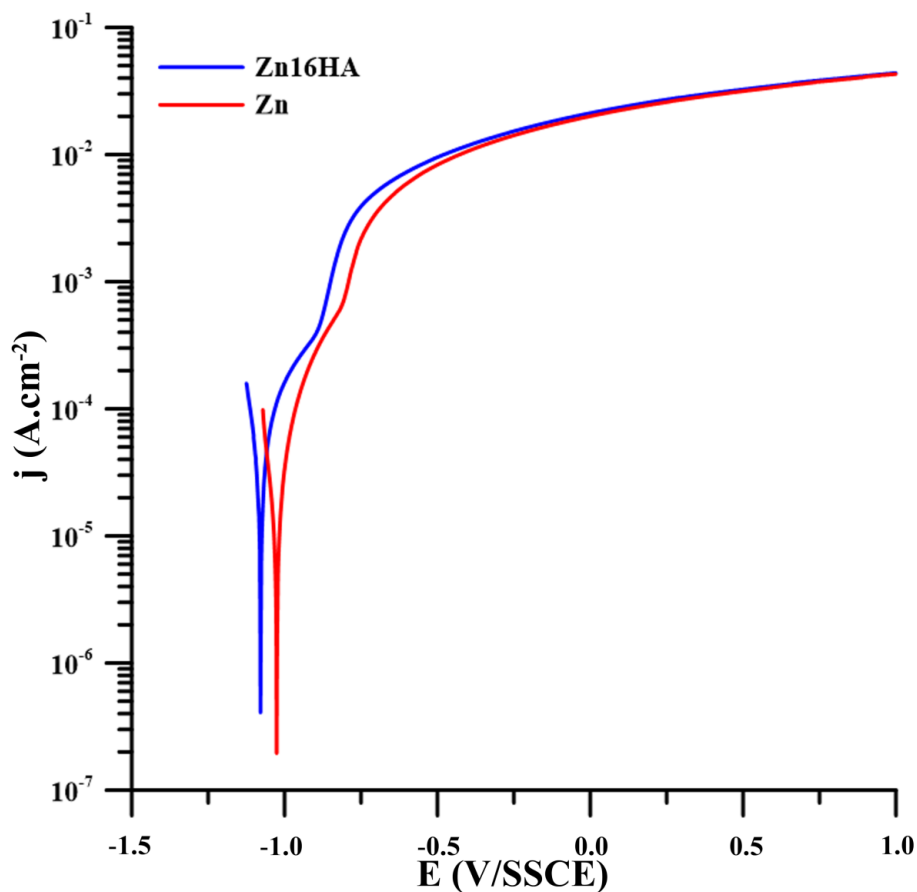


Figure 13. Potentiodynamic measurement of pure Zn and Zn/HA measured in SBF27.

4. Conclusions

A zinc composite containing 16 wt % of hydroxyapatite was successfully prepared by the spark plasma sintering method. The porosity and microstructure of the prepared samples were investigated by various methods and were discussed in detail. By the combination of theoretical calculations and image analysis, the total porosity value of the composite was estimated to be 18%. In addition, compression (CYS = 46 MPa and UCS = 65 MPa) and (for the first time for these materials) flexural properties (UFS = 120 MPa) were measured. Despite the fact that the mechanical properties of the pure sintered zinc were higher, the Zn/HA composite still possessed mechanical properties suitable for the potential cancellous bone replacements. The corrosion rate of the studied materials was 0.2 and 0.4 mm per year for pure zinc and for the Zn/HA composite respectively. The amount of zinc ions released per day also predetermines the usability of this material in the human body from the point of view of biocompatibility.

Author Contributions: J.P. coordinated the work, compiled the paper and realized the microstructure characterization, mechanical tests and immersion test. J.K. participated in image processing. J.Č. and D.V. worked as the scientific supervisors, F.P. prepared the samples by SPS process, V.H. realized electrochemical measurements, P.V. evaluated the XRD results and I.S. realized the measurements connected with the mercury porosimetry. All authors have read and agreed to the published version of the manuscript.

Funding: This research was funded by Czech Science Foundation, grant number 18-06110S, specific university research (MSMT no. 21-SVV/2019) and Operational Program Research, Development and Education financed by European Structural and Investment Funds and the Czech Ministry of Education, Youth and Sports (Project No. SOLID21-CZ.02.1.01/0.0/0.0/16_019/0000760).

Conflicts of Interest: The funders had no role in the design of the study; in the collection, analyses, or interpretation of data; in the writing of the manuscript, and in the decision to publish the results. The authors declare no conflict of interest.

References

1. Zheng, Y.F.; Gu, X.N.; Witte, F. Biodegradable metals. *Mater. Sci. Eng. R: Rep.* **2014**, *77*, 1–34. [\[CrossRef\]](#)
2. Moravej, M.; Mantovani, D. Biodegradable Metals for Cardiovascular Stent Application: Interests and New Opportunities. *Int. J. Mol. Sci.* **2011**, *12*, 4250. [\[CrossRef\]](#) [\[PubMed\]](#)
3. Sajjadi, S.A.; Ezatpour, H.R.; Torabi Parizi, M. Comparison of microstructure and mechanical properties of A356 aluminum alloy/Al₂O₃ composites fabricated by stir and compo-casting processes. *Mater. Des.* **2012**, *34*, 106–111. [\[CrossRef\]](#)
4. Conner, R.D.; Dandliker, R.B.; Johnson, W.L. Mechanical properties of tungsten and steel fiber reinforced Zr₄₁Ti₁₃75Cu₁₂5Ni₁₀Be₂₂5 metallic glass matrix composites. *Acta Mater.* **1998**, *46*, 6089–6102. [\[CrossRef\]](#)
5. Gleeson, J.P.; Plunkett, N.A.; O'Brien, F.J. Addition of hydroxyapatite improves stiffness, interconnectivity and osteogenic potential of a highly porous collagen-based scaffold for bone tissue regeneration. *Eur. Cells Mater.* **2010**, *20*, 218–230. [\[CrossRef\]](#)
6. Čapek, J.; Pinc, J.; Msallamová, Š.; Jablonská, E.; Veřtát, P.; Kubásek, J.; Vojtěch, D. Thermal plasma spraying as a new approach for preparation of zinc biodegradable scaffolds: A complex material characterization. *J. Therm. Spray Technol.* **2019**, *28*, 826–841. [\[CrossRef\]](#)
7. Ryan, G.; Pandit, A.; Apatsidis, D.P. Fabrication methods of porous metals for use in orthopaedic applications. *Biomaterials* **2006**, *27*, 2651–2670. [\[CrossRef\]](#)
8. Song, G.; Atrens, A.; Dargusch, M. Influence of microstructure on the corrosion of diecast AZ91D. *Corros. Sci.* **1998**, *41*, 249–273. [\[CrossRef\]](#)
9. Čapek, J.; Jablonská, E.; Lipov, J.; Kubatík, T.F.; Vojtěch, D. Preparation and characterization of porous zinc prepared by spark plasma sintering as a material for biodegradable scaffolds. *Mater. Chem. Phys.* **2018**, *203*, 249–258. [\[CrossRef\]](#)
10. Munir, Z.A.; Anselmi-Tamburini, U.; Ohyanagi, M. The effect of electric field and pressure on the synthesis and consolidation of materials: A review of the spark plasma sintering method. *J. Mater. Sci.* **2006**, *41*, 763–777. [\[CrossRef\]](#)
11. Sairam, K.; Sonber, J.K.; Murthy, T.S.R.C.; Subramanian, C.; Fotedar, R.K.; Nanekar, P.; Hubli, R.C. Influence of spark plasma sintering parameters on densification and mechanical properties of boron carbide. *Int. J. Refract. Metals Hard Mater.* **2014**, *42*, 185–192. [\[CrossRef\]](#)
12. Nouri, A.; Hodgson, P.D.; Wen, C.E. Effect of process control agent on the porous structure and mechanical properties of a biomedical Ti–Sn–Nb alloy produced by powder metallurgy. *Acta Biomater.* **2010**, *6*, 1630–1639. [\[CrossRef\]](#) [\[PubMed\]](#)
13. Joschek, S.; Nies, B.; Krotz, R.; Göpferich, A. Chemical and physicochemical characterization of porous hydroxyapatite ceramics made of natural bone. *Biomaterials* **2000**, *21*, 1645–1658. [\[CrossRef\]](#)
14. Matsunaga, K.; Murata, H.; Mizoguchi, T.; Nakahira, A. Mechanism of incorporation of zinc into hydroxyapatite. *Acta Biomater.* **2010**, *6*, 2289–2293. [\[CrossRef\]](#) [\[PubMed\]](#)
15. Koempel, J.A.; Patt, B.S.; O'Grady, K.; Wozney, J.; Toriumi, D.M. The effect of recombinant human bone morphogenetic protein-2 on the integration of porous hydroxyapatite implants with bone. *J. Biomed. Mater. Res.* **1998**, *41*, 359–363. [\[CrossRef\]](#)
16. Arifin, A.; Sulong, A.B.; Muhamad, N.; Syarif, J.; Ramli, M.I. Material processing of hydroxyapatite and titanium alloy (HA/Ti) composite as implant materials using powder metallurgy: A review. *Mater. Des.* **2014**, *55*, 165–175. [\[CrossRef\]](#)
17. White, A.A.; Best, S.M.; Kinloch, I.A. Hydroxyapatite–Carbon Nanotube Composites for Biomedical Applications: A Review. *Int. J. Appl. Ceram. Tec.* **2007**, *4*, 1–13. [\[CrossRef\]](#)
18. Sun, L.; Berndt, C.C.; Gross, K.A.; Kucuk, A. Material fundamentals and clinical performance of plasma-sprayed hydroxyapatite coatings: A review. *J. Biomed. Mater. Res.* **2001**, *58*, 570–592. [\[CrossRef\]](#)

19. Dehestani, M.; Adolfsson, E.; Stanciu, L.A. Mechanical properties and corrosion behavior of powder metallurgy iron-hydroxyapatite composites for biodegradable implant applications. *Mater. Des.* **2016**, *109*, 556–569. [[CrossRef](#)]
20. Witte, F.; Feyerabend, F.; Maier, P.; Fischer, J.; Störmer, M.; Blawert, C.; et al. Biodegradable magnesium–hydroxyapatite metal matrix composites. *Biomaterials* **2007**, *28*, 2163–2174. [[CrossRef](#)]
21. Ratna Sunil, B.; Ganapathy, C.; Sampath Kumar, T.S.; Chakkingal, U. Processing and mechanical behavior of lamellar structured degradable magnesium–hydroxyapatite implants. *J. Mech. Behav. Biomed. Mater.* **2014**, *40*, 178–189. [[CrossRef](#)] [[PubMed](#)]
22. Ulum, M.F.; Arafat, A.; Noviana, D.; Yusop, A.H.; Nasution, A.K.; Abdul Kadir, M.R.; Hermawan, H. In vitro and in vivo degradation evaluation of novel iron-bioceramic composites for bone implant applications. *Mater. Sci. Eng. C* **2014**, *36*, 336–344. [[CrossRef](#)] [[PubMed](#)]
23. Yang, H.; Qu, X.; Lin, W.; Wang, C.; Zhu, D.; Dai, K.; Zheng, Y. In vitro and in vivo studies on zinc-hydroxyapatite composites as novel biodegradable metal matrix composite for orthopedic applications. *Acta Biomater.* **2018**, *71*, 200–214. [[CrossRef](#)] [[PubMed](#)]
24. Levy, G.K.; Goldman, J.; Aghion, E. The Prospects of Zinc as a Structural Material for Biodegradable Implants-A Review Paper. *Metals* **2017**, *7*, 18.
25. Gong, H.B.; Wang, K.; Strich, R.; Zhou, J.G. In vitro biodegradation behavior, mechanical properties, and cytotoxicity of biodegradable Zn-Mg alloy. *J. Biomed. Mater. Res. Part B* **2015**, *103*, 1632–1640. [[CrossRef](#)] [[PubMed](#)]
26. Pospisilova, I.; Vojtech, D. Zinc Alloys for Biodegradable Medical Implants. In *Materials Science Forum*; Longauerova, M., Zubko, P., Eds.; Metallography Xv Trans Tech. Publications Ltd: Stafa-Zurich, Switzerland, 2014; pp. 457–460.
27. Katarivas Levy, G.; Leon, A.; Kafri, A.; Ventura, Y.; Drelich, J.W.; Goldman, J.; Vago, R.; Aghion, E. Evaluation of biodegradable Zn-1%Mg and Zn-1%Mg-0.5%Ca alloys for biomedical applications. *J. Mater. Sci. Mater. Med.* **2017**, *28*, 174. [[CrossRef](#)]
28. Gower-Winter, S.D.; Levenson, C.W. Zinc in the central nervous system: From molecules to behavior. *Biofactors* **2012**, *38*, 186–193. [[CrossRef](#)]
29. Cerovic, A.; Miletic, I.; Sobajic, S.; Blagojevic, D.; Radusinovic, M.; El-Sohemy, A. Effects of zinc on the mineralization of bone nodules from human osteoblast-like cells. *Biol. Trace Elem. Res.* **2007**, *116*, 61–71. [[CrossRef](#)]
30. Yamaguchi, M. Role of zinc in bone formation and bone resorption. *J. Trace Elem. Exp. Med.* **1998**, *11*, 119–135. [[CrossRef](#)]
31. Vojtěch, D.; Kubásek, J.; Šerák, J.; Novák, P. Mechanical and corrosion properties of newly developed biodegradable Zn-based alloys for bone fixation. *Acta Biomater.* **2011**, *7*, 3515–3522. [[CrossRef](#)]
32. Bowen, P.K.; Drelich, J.; Goldman, J. Zinc Exhibits Ideal Physiological Corrosion Behavior for Bioabsorbable Stents. *Adv. Mater.* **2013**, *25*, 2577–2582. [[CrossRef](#)] [[PubMed](#)]
33. Vojtěch, D.; Kubásek, J.; Čapek, J.; Pospíšilová, I. Comparative mechanical and corrosion studies on magnesium, zinc and iron alloys as biodegradable metals. *Mater. Tehnol.* **2015**, *49*, 877–882. [[CrossRef](#)]
34. Yong, L.; Wei, X.; Chengcheng, Z.; Biao, G.; Hanfeng, G.; Hao, C.; Fu, J.; Feng, L. Enhanced osseointegration and antibacterial action of zinc-loaded titania-nanotube-coated titanium substrates: In vitro and in vivo studies. *J. Biomed. Mater. Res. Part A* **2014**, *102*, 3939–3950.
35. Ann, L.C.; Mahmud, S.; Bakhori, S.K.M.; Sirelkhatim, A.; Mohamad, D.; Hasan, H.; Seeni, A.; Rahman, R.A. Antibacterial responses of zinc oxide structures against *Staphylococcus aureus*, *Pseudomonas aeruginosa* and *Streptococcus pyogenes*. *Ceram. Int.* **2014**, *40*, 2993–3001. [[CrossRef](#)]
36. Soon, L.L.; Zuhailawati, H.; Suhaina, I.; Dhindaw, B.K. Prediction of Compressive Strength of Biodegradable Mg–Zn/HA Composite via Response Surface Methodology and Its Biodegradation. *Acta Metall. Sin.* **2016**, *29*, 464–474. [[CrossRef](#)]
37. Salleh, E.M.; Zuhailawati, H.; Ramakrishnan, S.; Dhindaw, B.K. Enhanced Mechanical Properties and Corrosion Behavior of Biodegradable Mg–Zn/HA Composite. *Metall. Mater. Trans. A* **2017**, *48*, 2519–2528. [[CrossRef](#)]
38. Yang, F.; Dong, W.J.; He, F.M.; Wang, X.X.; Zhao, S.F.; Yang, G.L. Osteoblast response to porous titanium surfaces coated with zinc-substituted hydroxyapatite. *Oral Surg. Oral Med. Oral Pathol. Oral Radiol.* **2012**, *113*, 313–318. [[CrossRef](#)]

39. Candidato, R.T.; Thouzellier, C.; Pawlowski, L. Evaluation of the in-vitro behavior of nanostructured hydroxyapatite and zinc doped hydroxyapatite coatings obtained using solution precursor plasma spraying. *J. Biomed. Mater. Res. Part B Appl. Biomater.* **2017**, *106*, 2101–2108. [\[CrossRef\]](#)
40. Uysal, I.; Severcan, F.; Tezcaner, A.; Evis, Z. Co-doping of hydroxyapatite with zinc and fluoride improves mechanical and biological properties of hydroxyapatite. *Prog. Nat. Sci. Mater. Int.* **2014**, *24*, 340–349. [\[CrossRef\]](#)
41. Yuan, Q.; Wu, J.; Qin, C.; Xu, A.; Zhang, Z.; Lin, Y.; Chen, Z.; Lin, S.; Yuan, Z.; Ren, X.; et al. One-pot synthesis and characterization of Zn-doped hydroxyapatite nanocomposites. *Mater. Chem. Phys.* **2017**, *199*, 122–130. [\[CrossRef\]](#)
42. Müller, L.; Müller, F.A. Preparation of SBF with different HCO₃⁻ content and its influence on the composition of biomimetic apatites. *Acta Biomater.* **2006**, *2*, 181–189. [\[CrossRef\]](#) [\[PubMed\]](#)
43. Thümmel, F.; Oberacker, R. Porosity and Pore-related properties. In *Introduction to Powder Metallurgy*; Maney Publishing for IOM3; The Institute of Materials, Minerals and Mining: London, UK, 1993; ISBN 978-0-901716-26-2.
44. Zhang, L.; He, Z.Y.; Zhang, Y.Q.; Jiang, Y.H.; Zhou, R. Rapidly sintering of interconnected porous Ti-HA biocomposite with high strength and enhanced bioactivity. *Mater. Sci. Eng. C* **2016**, *67*, 104–114. [\[CrossRef\]](#)
45. Silva, V.V.; Domingues, R.Z.; Lameiras, F.S. Microstructural and mechanical study of zirconia-hydroxyapatite (ZH) composite ceramics for biomedical applications. *Compos. Sci. Technol.* **2001**, *61*, 301–310. [\[CrossRef\]](#)
46. Wu, S.; Liu, X.; Yeung, K.W.K.; Liu, C.; Yang, X. Biomimetic porous scaffolds for bone tissue engineering. *Mater. Sci. Eng. R. Rep.* **2014**, *80*, 1–36. [\[CrossRef\]](#)
47. Zhang, X.; Li, X.W.; Li, J.G.; Sun, X.D. Preparation and mechanical property of a novel 3D porous magnesium scaffold for bone tissue engineering. *Mater. Sci. Eng. C* **2014**, *42*, 362–367. [\[CrossRef\]](#) [\[PubMed\]](#)
48. Čapek, J.; Vojtěch, D. Effect of sintering conditions on the microstructural and mechanical characteristics of porous magnesium materials prepared by powder metallurgy. *Mater. Sci. Eng. C* **2014**, *35*, 21–28. [\[CrossRef\]](#)
49. Del Campo, R.; Savoini, B.; Muñoz, A.; Monge, M.A.; Pareja, R. Processing and mechanical characteristics of magnesium-hydroxyapatite metal matrix biocomposites. *J. Mech. Behav. Biomed. Mater.* **2017**, *69*, 135–143. [\[CrossRef\]](#) [\[PubMed\]](#)
50. Lee, Y.J.; Elzinga, E.J.; Reeder, R.J. Sorption Mechanisms of Zinc on Hydroxyapatite: Systematic Uptake Studies and EXAFS Spectroscopy Analysis. *Environ. Sci. Technol.* **2005**, *39*, 4042–4208. [\[CrossRef\]](#)
51. Wei, X.; Yates, M.Z. Yttrium-Doped Hydroxyapatite Membranes with High Proton Conductivity. *Chem. Mater.* **2012**, *24*, 1738–1743. [\[CrossRef\]](#)
52. Wellinghausen, N. Immunobiology of gestational zinc deficiency. *Br. J. Nutr.* **2007**, *85*, S81–S86. [\[CrossRef\]](#)
53. Kokubo, T.; Takadama, H. How useful is SBF in predicting in vivo bone bioactivity? *Biomaterials* **2006**, *27*, 2907–2915. [\[CrossRef\]](#) [\[PubMed\]](#)
54. Liu, L.; Meng, Y.; Dong, C.; Yan, Y.; Volinsky, A.A.; Wang, L.N. Initial formation of corrosion products on pure zinc in simulated body fluid. *J. Mater. Sci. Technol.* **2018**, *34*, 2271–2282. [\[CrossRef\]](#)
55. Turianicová, E.; Kaňuchová, M.; Zorkovská, A.; Holub, M.; Bujňáková, Z.; Dutková, E.; Baláž, M.; Findoráková, L.; Balintová, M.; Obut, A. CO₂ utilization for fast preparation of nanocrystalline hydrozincite. *J. CO₂ Util.* **2016**, *16*, 328–335. [\[CrossRef\]](#)
56. Mahmoudian, M.R.; Basirun, W.J.; Alias, Y.; Ebadi, M. Facile fabrication of Zn/Zn₅(OH)₈Cl₂·H₂O flower-like nanostructure on the surface of Zn coated with poly (N-methyl pyrrole). *Appl. Surf. Sci.* **2011**, *257*, 10539–10544. [\[CrossRef\]](#)
57. Hu, Q.; Zhang, G.; Qiu, Y.; Guo, X. The crevice corrosion behaviour of stainless steel in sodium chloride solution. *Corros. Sci.* **2011**, *53*, 4065–4672. [\[CrossRef\]](#)

